VOL. 12, NO. 24, DECEMBER 2017 ISSN 1819-6608
ARPN Journal of Engineering and Applied Sciences

www.arpnjournals.com

KINEMATIC COMPUTATIONS FOR SMALL-SIZE HUMANOID ROBOT KUBO

E. Hernández[1], R. Velázquez[1], R. Macías-Quijas[1], E. Pissaloux[2], N. I. Giannoccaro[3] and A. Lay-Ekuakille[3]
[1]Universidad Panamericana. Facultad de Ingeniería, Aguascalientes, Mexico
[2]Université de Rouen. Département Physique, Mont-Saint-Aignan, France
[3]Università del Salento, Dipartimentod' Ingegneriadell'Innovazione, Lecce, Italy
E-Mail: rvelazquez@up.edu.mx

ABSTRACT

This paper overviews the kinematics and workspace computer simulation of a small-size humanoid robot named KUBO. This bipedal walking platform has 20 degrees of freedom (DOF) and is powered by servomotors that perform reliable torque and precise motion. Made entirely from aluminum and assembled with commercial off-the-shelf actuators and sensors, KUBO is a self-developed low-cost platform for research into humanoid robots, human-like motion, bipedal walking, and control. It is capable of moving forward, backward, sideway, it can turn in any direction, lie down, and get up. In addition, it performs object tracking and recognition using an on-board video camera. In this paper, the design, implementation, mechanical analysis, and vision capabilities of this prototype are presented and discussed.

Keywords: ball tracking, effective workspace, humanoid robot, kinematic computations, robot limbs.

1. INTRODUCTION

Over the last decade, there has been a growing interest in humanoid robots and biped motion. This is certainly due to new needs and expectations humans have from robots. It seems that requirements for factory automation, assembly, and industrial process control have been reasonably fulfilled. However, new fields such as service and assistive robotics require different kinds of robots that humans can interact with. Humanoid robots have strongly emerged as human friendly systems because of their anthropomorphism, friendly appearance and interaction, high applicability in human environments, etc.

Within this context, several humanoid robots have been developed in the last years. Some representative examples are the H6 and H7 humanoid robots of the University of Tokyo [1], Johnnie of the Technical University of Munich [2], the HRP series of AIST/Kawada Industries [3], and the well-known Honda's ASIMO robot [4]. All these impressive platforms are with no doubt high-tech complex systems that require a considerable investment from universities and research institutes. In consequence, few well-funded laboratories worldwide have one of these prototypes. Researchers working in different aspects of humanoid robotics have to find collaboration with these laboratories in order to test their work. Unfortunately, collaboration and schedule times are not always successful.

Since 2003, small affordable humanoid robots have appeared and are commercially available at very competitive prices (for example, Sony's SDR-3X [5] the Kondo robot [6], the Nao robot [7], the Robotinno [8], the DARwIn-OP [9], theHOAP-2 [10], etc.). These prototypes are usually 30-40 cm height and offer between 16-19 DOF. These products are attractive platforms for hobbyists and beginners into humanoid robots and robotics education. Their main drawback is that they are not immediately suitable for research because their mechanical structures are not flexible (ie. they cannot be modified), the number and types of on-board sensors may be not enough to enable

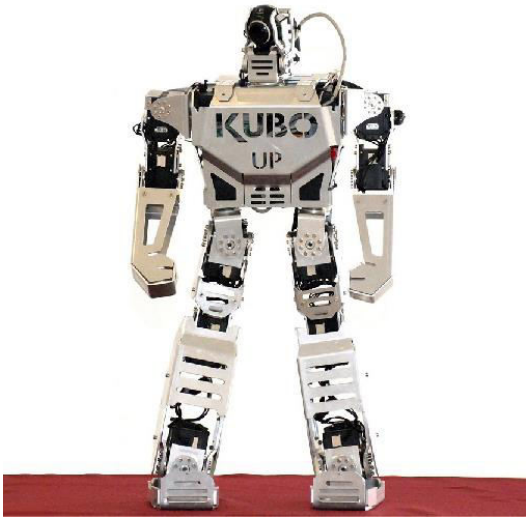

Figure-1. Humanoid robot KUBO.

effective feedback for balance and walking, and they lack of sufficient on-board computing and processing power.

To overcome these limitations, we have chosen to design and develop our own prototype of humanoid robot. KUBO is a servo-driven humanoid robot that offers 20 DOF (Figure-1). Its structure consists of complex aluminum links manufactured with ultra-high precision to reduce backlashes/misalignments and achieve precise motion. KUBO is taller than commercially available robots (60 cm) and includes an on-board video camera, ample on-board computing power, and a number of sensors that allow the development of control strategies for standing balance and walking.

The rest of the paper is organized as follows: Section 2 introduces the hardware development,

describing comprehensively the mechanical design, kinematic structure, and sensors and actuators contained in the prototype. Section 3 presents a comprehensive kinematic analysis of humanoid robot KUBO. Section 4 overviews its vision capabilities in particular for one application: playing

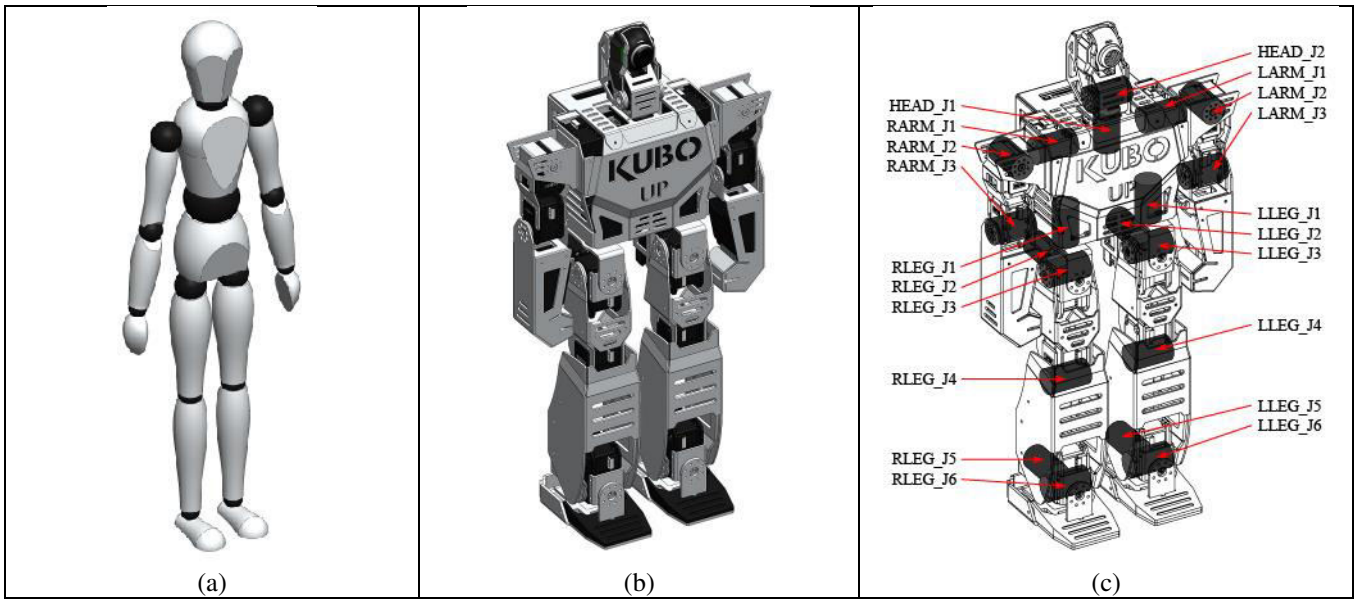

(a) (b) (c)

Figure-2. Humanoid robot KUBO: (a) design based on the biomechanical human model, (b) conceptual representation, and (c) kinematic structure with labels identifying all joints.

soccer. Finally, the conclusion summarizes the main contributions and future work perspectives.

2. PROTOTYPE OVERVIEW

A) Design and implementation

KUBO is a humanoid robotic platform designed to be compact, lightweight, robust, and highly performant. It is the third version of humanoid robots we have developed. It integrates the technological improvements of the two previous prototypes: ZERO [11] and AXIS [12].

It is based on the biomechanical human model (Figure-2(a)), with an anthropomorphic structure containing a head, a torso, two arms, and two legs. Its overall design is shown in Figure-2(b).

All links of KUBO's mechanical structure were made from two types of aluminum alloys: 3105-H22 and 3003-H23. The first one is malleable and was used for the most complex links containing folds. The second one is rigid and was used for the simpler links. H22 aluminum links were laser cut with a ±2 micron precision, folded with hydraulic press, and welded using gas tungsten arc welding. H23 aluminum links were manufactured with a three-axis CNC machine.

Actuators powering KUBO's joints are servo motors of type RX-28 and RX-64 from Dynamixel [13]. Both types of servo motors provide a step precision of 0.29° and a 28 and 64 kgf-cm torque, respectively. RX-28 servo motors were used for the head and the upper limbs while RX-64 motors were used for the lower limbs.

The required power source to keep 20 min of KUBO's autonomy moving all actuators at maximum torque is obtained from two packages of rechargeable LiPo batteries of 18.5 V at 750 mA.

B) Kinematic structure

KUBO exhibits 20DOF powered by a total of 20 actuators. Its kinematic structure is detailed in Figure-2(c) while its degrees of freedom are listed in Table-1.

Table-1. DOF of humanoid robot KUBO.

Head	**Arms** (2)	**Legs** (2)	**Total**
2 (neck)	2 (shoulder)	3 (hips)	
	1 (elbow)	1 (knee)	
		2 (ankle)	
2 DOF	6-DOF	12-DOF	20-DOF

The head consists of a pan-and-tilt structure attached to a neck (2-DOF). Arms add 6-DOF, 3-DOF each: two at shoulder level allowing roll and pitch rotations and one at the elbow. Finally, the legs add 12-DOF, 6-DOF each: three at the upper level that allow full rotation of the entire leg (roll, pitch, and yaw), one at the knee, and two at the ankle. Head, arms, and legs are mounted on a torso.

C) Electrical drive

Figure-3 shows KUBO's connection block diagram. The main structure involves four types of blocks connected to each other by electrical and data lines. These

blocks represent components, sensors, and the upper and lower actuators, which form together KUBO's hardware.

On the upper side, there are eight servo motors RX-28 (blue), three for each arm (3-DOF) and two for the head (2-DOF), while in the lower side there are 12 servo motors RX-64 (green): six for each leg (6-DOF). Since the actuators on the lower side require a higher torque (because of the weight they have to move), a higher voltage needs to be supplied (green line). On the upper side, the torque is minimum and a lower voltage (blue line) can be supplied.

Three types of sensors (orange) are used to have feedback from the outer world: a webcam placed on the head's pan-and-tilt structure, that allows object tracking, a digital compass located inside the chest, which includes magnetic sensors and accelerometers that let the robot know whether it is lied down up face or down face, and finally, force sensors placed in the feet soles to keep the robot's balance. The processing unit is located inside KUBO's torso, and is mainly used for image processing and servo motor control.

Likewise, instructions for the actuators are sent by the processing unit through a servo motor controller. Data are sent by serial connection (black line) all along the 20 servo motors, even if some at the middle of the chain are not required to move. The main power source of the robot is taken from the batteries placed inside the arms (green line).

3. KINEMATIC ANALYSIS

In order to predict KUBO's motion, it is important to first analyze its kinematics. Since the general kinematic structures of the left arm/leg of the prototype are identical to those of the right arm/leg, only the right limbs will be discussed. Left side solutions can be obtained by just switching one vector's direction.

This section presents the kinematical modeling of KUBO's arms and legs.

A) Arm modeling

Figure-4(a) shows the structure of the right arm. As aforementioned, each arm is a 3-DOF structure powered by three actuators. Note that servo motors powering the shoulder and the arm share a common axis of rotation.

In Figure-4(a), the base frame Σ_B represents axis (x_B, y_B, z_B) and is the coordinate reference frame of the entire arm. Frames Σ_0, Σ_1, and Σ_2, are the local axes of the links while Σ_3 is the frame located at the end effector. Revolute joints connect all links. Their rotation is denoted by θ_i. Distance between Σ_B and Σ_0 is a_0, while the length of each link is denoted by a_i. The objective is to find the position and orientation of the end effector's frame with respect to the base frame. This can be achieved by establishing a forward kinematic model that estimates resultant vector $\boldsymbol{p_3^B}$.

Inspired by the kinematics of robot manipulators [14-15], the position p_3^B of the end effector can be expressed in both Σ_B and Σ_3 by Equation (1):

$$\sum B = R \sum 3 \tag{1}$$

Where R is the rotation matrix that represents the transformation of coordinates in frame Σ_3 into the coordinates of frame Σ_B. To obtain R, the use of the homogeneous transformation matrix Equation (2) can be considered:

$$\mathbf{A}_n^{n-1}(\theta_n) = \begin{bmatrix} R_n^{n-1} & p_n^{n-1} \\ 0^T & 1 \end{bmatrix} = \begin{bmatrix} \mathbf{n} & \mathbf{s} & \mathbf{a} & \mathbf{p} \\ 0 & 0 & 0 & 1 \end{bmatrix} \tag{2}$$

Where A_n^{n-1} is the transformation matrix from link n-1 to link n. Matrix A is a function of θ_n. R_n^{n-1} is a 3x3 matrix representing rotation while p_n^{n-1} is a 3x1 matrix representing translation. The right-hand side [n s a p] represents the normal vector, the sliding vector, the approach vector, and the position vector of the end effector, respectively. Denavit-Hartenberg parameters for KUBO's right arm are listed in Table-2.

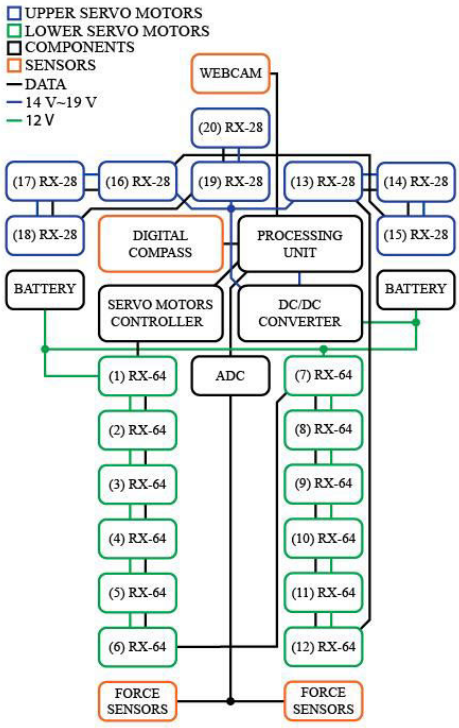

Figure-3. Connection block diagram of humanoid robot KUBO.

Table-2. Denavit-Hartenberg parameters of the arm.

Link	θ	d	a	α	Range of motion	
1	$-\pi/2$	0	0	$-\pi/2$	-90°	+180°
2	0	0	a_2	$\pi/2$	-180°	0°
3	0	0	a_3	0	0°	+95°

Thus, Equation. (2) becomes Equation. (3):

$$\mathbf{A}_n^{n-1}(\theta_n) = \begin{bmatrix} C_n & -S_n C_{\alpha_n} & S_n S_{\alpha_n} & a_n C_n \\ S_n & C_n C_{\alpha_n} & -C_n S_{\alpha_n} & a_n S_n \\ 0 & S_n & C_{\alpha_n} & d_n \\ 0 & 0 & 0 & 1 \end{bmatrix} \quad (3)$$

Where$C_n = \cos(\theta_n)$, $S_n = \sin(\theta_n)$, $C_{\alpha_n} = \cos(\alpha_n)$, and $S_{\alpha_n} = \sin(\alpha_n)$.

Due to the fact that the first link of the arm starts from the shoulder joint, the transformation matrix from the base frame attached to the torso to the first coordinate frame of the right arm is Equation (4):

$$\mathbf{A}_0^B = \begin{bmatrix} 0 & 0 & 1 & a_0 \\ 1 & 0 & 0 & 0 \\ 0 & 1 & 0 & 0 \\ 0 & 0 & 0 & 1 \end{bmatrix} \quad (4)$$

In order to describe the rotational and translational relationship between adjacent links, the Denavit-Hartenberg (D-H) matrix representation for each link must be used.

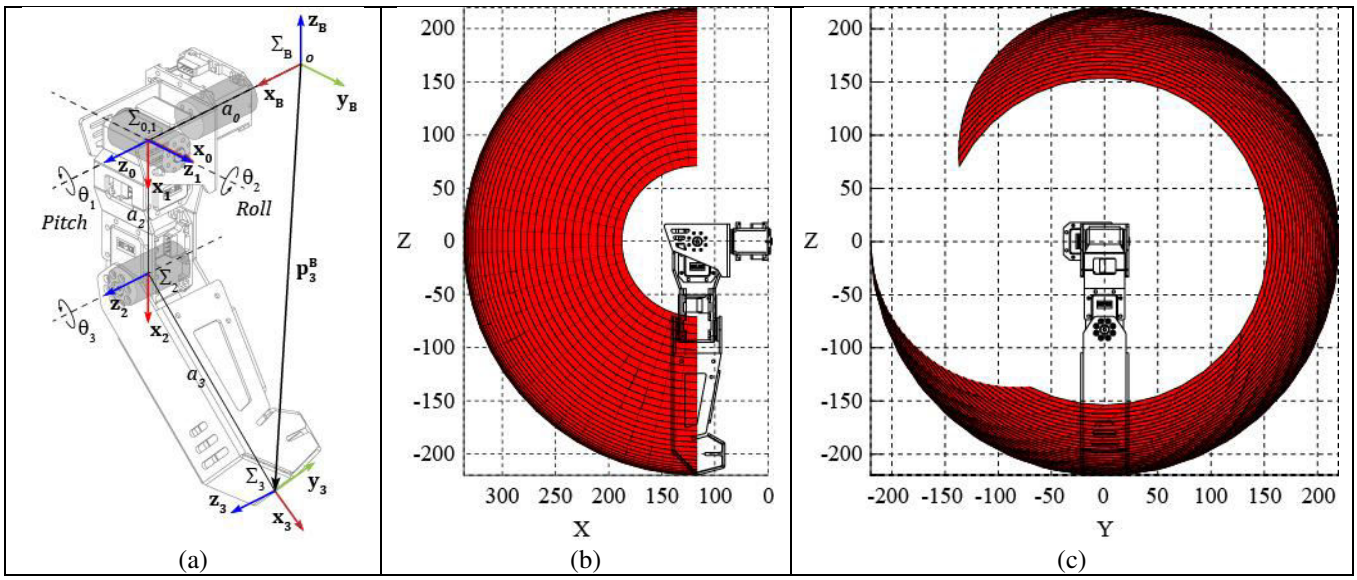

Figure-4. KUBO's right arm modelling: (a) link coordinate frames, (b) roll workspace, and (c) pitch workspace defined by the space between the maximum and minimum reach limits. All scales in [mm].

Thus, substituting parameters of Table-2 into Equation. (3) gives a set of transformation matrices for all links (Equations. (5) to (7)).
forn=1, transformation matrix of Σ_1 with respect to Σ_0 gives Equation (5):

$$\mathbf{A}_1^0(\theta_n) = \begin{bmatrix} C_1 & 0 & -S_1 & 0 \\ S_1 & 0 & C_1 & 0 \\ 0 & -1 & 0 & 0 \\ 0 & 0 & 0 & 1 \end{bmatrix} \quad (5)$$

forn=2, transformation matrix of Σ_2 with respect to Σ_1 gives Equation. (6)

$$\mathbf{A}_2^1(\theta_2) = \begin{bmatrix} C_2 & 0 & S_2 & a_2 C_2 \\ S_2 & 0 & -C_2 & a_2 S_2 \\ 0 & 1 & 0 & 0 \\ 0 & 0 & 0 & 1 \end{bmatrix} \quad (6)$$

forn=3, transformation matrix of Σ_3 with respect to Σ_2 gives Equation (7):

$$\mathbf{A}_3^2(\theta_n) = \begin{bmatrix} C_3 & -S_3 & 0 & a_3 C_3 \\ S_3 & C_3 & 0 & a_3 S_3 \\ 0 & 0 & 1 & 0 \\ 0 & 0 & 0 & 1 \end{bmatrix} \quad (7)$$

The forward kinematics $\boldsymbol{T_3^B}$ is then established by chain-multiplying the consecutive transformations matrices $\boldsymbol{A_n^{n-1}}$ (Equation (8)):

$$\mathbf{T}_3^B = \mathbf{A}_0^B\mathbf{A}_1^0\mathbf{A}_2^1\mathbf{A}_3^2 = \begin{bmatrix} \mathbf{n}_x & \mathbf{s}_x & \mathbf{a}_x & \mathbf{p}_x \\ \mathbf{n}_y & \mathbf{s}_y & \mathbf{a}_y & \mathbf{p}_y \\ \mathbf{n}_z & \mathbf{s}_z & \mathbf{a}_z & \mathbf{p}_z \\ 0 & 0 & 0 & 1 \end{bmatrix} \quad (8)$$

Where:

$$\mathbf{n}_x = -S_2C_3$$
$$\mathbf{n}_y = C_1C_2C_3 - S_1S_3$$
$$\mathbf{n}_z = S_1C_2C_3 + C_1S_3$$
$$\mathbf{s}_x = S_2S_3$$
$$\mathbf{s}_y = -C_1C_2S_3 - S_1C_3$$
$$\mathbf{s}_z = -S_1C_2S_3 + C_1C_3$$
$$\mathbf{a}_x = C_2$$
$$\mathbf{a}_y = C_1S_2$$
$$\mathbf{a}_z = S_1S_2$$
$$\mathbf{p}_x = a_0 - a_2S_2 - a_3S_2C_3$$
$$\mathbf{p}_y = a_2C_1C_2 + a_3(C_1C_2C_3 - S_1S_3)$$
$$\mathbf{p}_z = a_2S_1C_2 + a_3(S_1C_2C_3 + C_1S_3)$$

Vector $\boldsymbol{p_3^B}$ is defined by the translation components of matrix$\boldsymbol{T_3^B}$. These are Equation (9):

$$\mathbf{p}_3^B = \begin{bmatrix} \mathbf{p}_x \\ \mathbf{p}_y \\ \mathbf{p}_z \end{bmatrix} = \begin{bmatrix} a_0 - a_2S_2 - a_3S_2C_3 \\ a_2C_1C_2 + a_3(C_1C_2C_3 - S_1S_3) \\ a_2S_1C_2 + a_3(S_1C_2C_3 + C_1S_3) \end{bmatrix} \quad (9)$$

Simulation of Equation (9) provides a visualization of KUBO's right arm's reachable workspace. Figure-4(b) shows the arm roll workspace while Figure-4(c) shows the pitch workspace. The space between both plots is the effective workspace. Simulations show no collision against the robot itself.

B) Leg modeling

Figure-5 shows the structure of the right leg. Each leg is a 6-DOF structure powered by six servomotors, creating the joints of the hip, crotch, thigh, knee, ankle, and foot. The leg can be considered a spherical manipulator at the three upper joints and an anthropomorphic manipulator at the three lower ones. Note that motors powering the hip, crotch, and thigh share a common axis of rotation, while the ankle and foot share another one, thus obtaining a simplified kinematic model with lower variables to solve.

The objective is to find the position and orientation of the frame at the foot sole with respect to the frame at the base coordinate reference of the entire leg. As in the arm, this can be achieved by establishing a forward kinematic model that estimates resultant vector p_6^B expressed in both Σ_B and Σ_6:

$$\sum B = R \sum 6 \quad (10)$$

To obtain R, the use of the homogeneous transformation matrix A_n^{n-1} in Equation (2) can be considered again. D-H parameters for KUBO's right leg are listed in Table-3.

Table-3. Denavit-Hartenberg parameters of the leg.

Link	θ	d	a	α	Range of motion	
1	0	0	0	$\pi/2$	-37°	+143°
2	$\pi/2$	0	0	$-\pi/2$	-37°	+90°
3	0	0	a_3	0	-52°	+118°
4	0	0	a_4	0	-140°	0°
5	0	0	0	$\pi/2$	-45°	+90°
6	0	0	a_6	0	-22°	+22°

As in the arm, the transformation matrix from the base frame attached to the coordinate reference to the first frame of the right leg is given by Equation (11):

$$\mathbf{A}_0^B = \begin{bmatrix} -1 & 0 & 0 & a_0 \\ 0 & 1 & 0 & 0 \\ 0 & 0 & -1 & 0 \\ 0 & 0 & 0 & 1 \end{bmatrix} \quad (11)$$

By substituting parameters of Table-3 into Equation (3), transformation matrices can be derived for all the links.

for n=1,5, transformation matrices are given by Equation (12):

$$\mathbf{A}_n^{n-1}(\theta_n) = \begin{bmatrix} C_n & 0 & S_n & 0 \\ S_n & 0 & -C_n & 0 \\ 0 & 1 & 0 & 0 \\ 0 & 0 & 0 & 1 \end{bmatrix} \quad (12)$$

While transformation matrices for n=2 and n=3, 4, 6 are the same of those of Equation (5) and Equation (7), respectively.

The forward kinematics of the upper part of the leg $\boldsymbol{T_3^0}$ is thus defined by Equation (13):

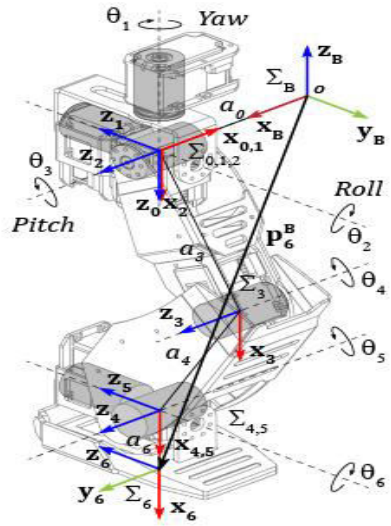

Figure-5. Link coordinate frames of KUBO's right leg.

$$\mathbf{T}_3^0 = \mathbf{A}_1^0\mathbf{A}_2^1\mathbf{A}_3^2 = \begin{bmatrix} f_{11} & f_{12} & f_{13} & f_{14} \\ f_{21} & f_{22} & f_{23} & f_{24} \\ f_{31} & f_{32} & f_{33} & f_{34} \\ 0 & 0 & 0 & 1 \end{bmatrix} \quad (13)$$

Where:

$f_{11} = C_1C_2C_3 - S_1S_3$
$f_{21} = S_1C_2C_3 + C_1S_3$
$f_{31} = S_2C_3$
$f_{12} = -C_1C_2S_3 - S_1C_3$
$f_{22} = -S_1C_2S_3 + C_1C_3$
$f_{32} = -S_2S_3$
$f_{13} = -C_1S_2$
$f_{23} = -S_1S_2$
$f_{33} = C_2$
$f_{14} = a_3(C_1C_2C_3 - S_1S_3)$
$f_{24} = a_3(S_1C_2C_3 + C_1S_3)$
$f_{34} = a_3S_2C_3$

While the forward kinematics of the lower part of the leg $\boldsymbol{T_6^3}$ is defined by Equation (14):

$$\mathbf{T}_6^3 = \begin{bmatrix} C_{45}C_6 & -C_{45}S_6 & S_{45} & a_4C_4 + a_6C_{45}C_6 \\ S_{45}C_6 & -S_{45}S_6 & -C_{45} & a_4S_4 + a_6S_{45}C_6 \\ S_6 & C_6 & 0 & a_6S_6 \\ 0 & 0 & 0 & 1 \end{bmatrix} \quad (14)$$

Since the entire leg can be considered as a double manipulator (a spherical manipulator at the upper part and an anthropomorphic manipulator at the lower one), the forward kinematics equation of the leg can be defined by chain-multiplying Equation (11), Equation (13), and Equation (14):

$$\mathrm{T}_6^B = \mathrm{A}_0^B\mathrm{T}_3^0\mathrm{T}_6^3 \quad (15)$$

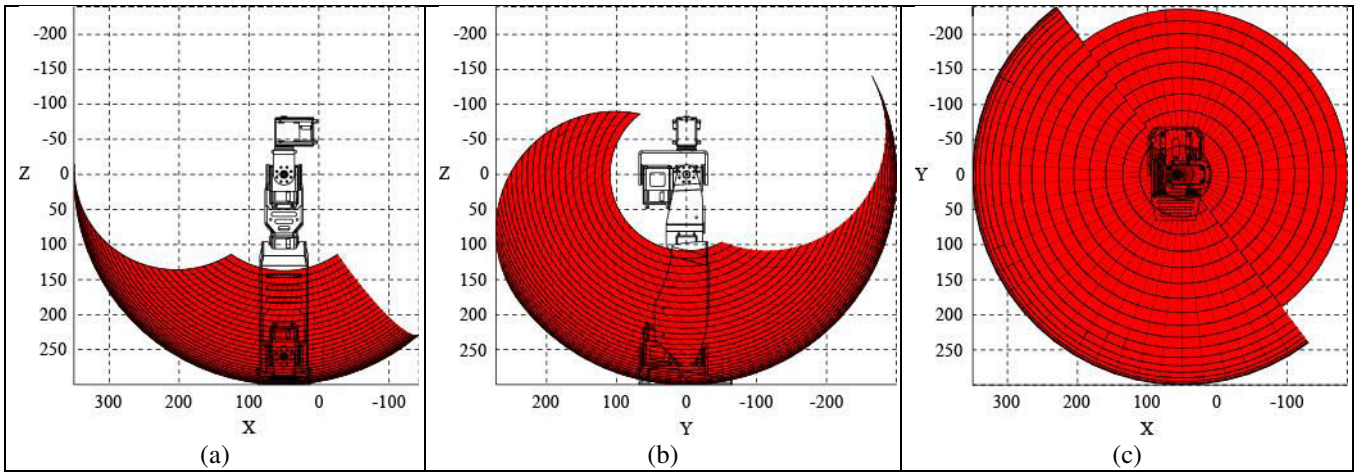

Figure-6. KUBO's right leg workspace defined by the space between the maximum and minimum reach limits: (a) roll,(b) pitch, and (c) yaw.All scales in [mm].

Solution of Equation (15) is indeed complex to express. However, as in the arm, vector p_6^B is defined by the translation components of matrixT_6^B. These are Equation (16):

$$\mathrm{p}_6^B = \begin{bmatrix} \mathrm{p}_x \\ \mathrm{p}_y \\ \mathrm{p}_z \end{bmatrix} = \begin{bmatrix} \mathrm{T}_{6\ 14}^B \\ \mathrm{T}_{6\ 24}^B \\ \mathrm{T}_{6\ 34}^B \end{bmatrix} \quad (16)$$

Simulation of Equation (16) provides a visualization of KUBO's right leg's reachable workspace. Figure-6(a) shows the leg roll workspace, Figure-6(b) shows the pitch workspace, and Figure-6(c) shows the yaw workspace. The space between all plots is the leg's effective workspace.

In this case, simulation shows the leg's workspaces intersection evidencing collisions, since the range of motion of servo motors allow wider movements increasing reachable space for the leg. In some cases, such

as when the robot turns over, the right leg overlaps the left leg's workspace but collision may be avoided by setting conditional parameters to the robot's motion control. This valuable information can be used to prevent the robot from harming itself while performing tasks.

It is possible to visualize KUBO's total roll workspace by simulating Equations. (9) and (16) at different coordinate references and overlapping the resulting plots. Figure-7(a) and (b) show the total roll workspace for the four limbs. The space between the four plots altogether define the effective roll workspace of the robot.

4. VISION CAPABILITIES

Some ambitious scientific initiatives, such as the one proposed by RoboCup [16], aim to accomplish by 2050 a team of fully autonomous humanoid robots that can work in cooperation and beat humans in physically demanding games like soccer.

This great challenge can only be achieved by developing robots with human-like behavior and reasoning [17]. To reach that level, artificial vision in humanoid robots must be capable of processing all the information captured by their vision sensors in order to know where the ball is, how fast it moves in the soccer field, and the movements required from the robot to score a goal.

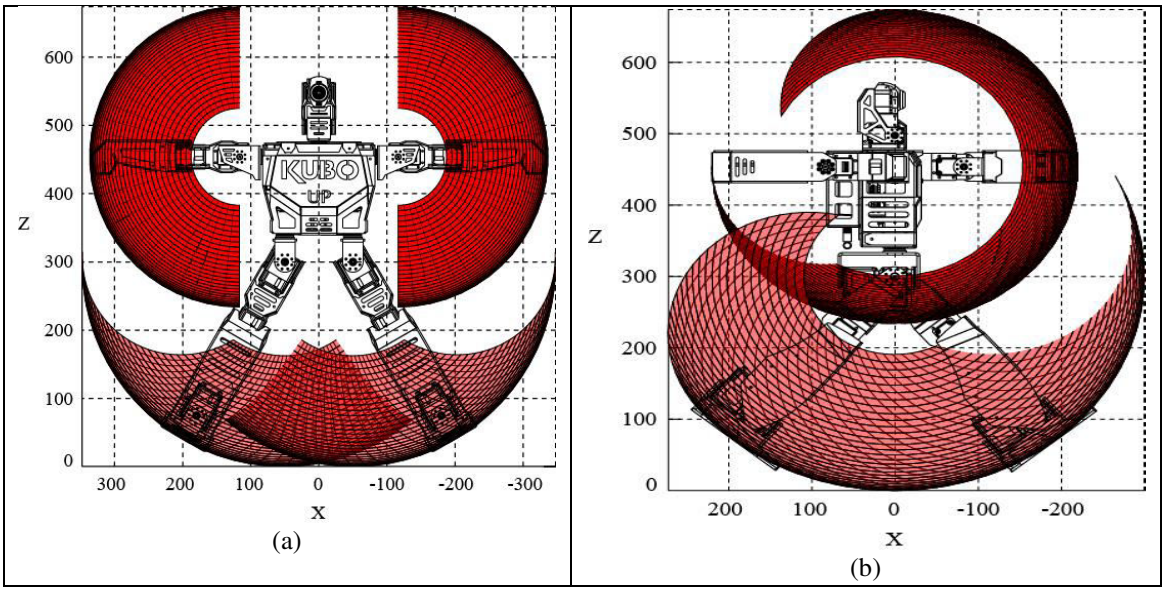

Figure-7. Total roll workspace defined by the space between the maximum and minimum reach limits of arms and legs: (a) frontal and (b) side view. All scales in [mm].

Within this context, this section presents a computer vision algorithm for locating balls of a specific color inside a soccer field under any type of illumination conditions - from a fully illuminated environment to partial darkness - using only the webcam located in KUBO's head.

This algorithm is composed of two main modules:

- Robust color detection under any type of illumination and
- Object recognition based on geometric features.

Modules are sequential and work in open loop (Figure-8).

A) Color detection

Once the images have been acquired by KUBO's camera, the algorithms proceeds with color detection. The main challenge in this first stage is the color variations in the image due to exterior lighting. The more light present in the environment, the greater the number of reflections and brightness in the objects. In contrast, as light decreases, the shadows increase in the image (and thus, less visibility). In order to detect a ball of a specific color under any external lighting condition, it is necessary to look for the target color in a range of variable intensities. Robust color detection can be achieved in four steps:

a) The initial conditions are first stablished; these are the acquired image and the real and ideal intensities for each band of the RGB image.

Inputs: I_m, R_r, R_i, G_r, G_i, B_r, B_i
Output: $I_{mf}[n]$

Where I_m is the original image and R, G, and B are its red, green, blue bands, respectively. The subscripts **r** and **i** stand for 'real' and 'ideal', respectively. I_{mf} is the final processed image in sample n.

b) Color sensitivity is then defined as a gradient in the RGB space (Equation (17)):

$$\nabla RGB \in (Rr \pm Ri)\, U\, (Gr \pm Gi)\, U\, (Br \pm Bi) \quad (17)$$

c) The method searchs for this gradient in the three bands of the RGB image using Equation (18):

$$\sum_{n=0}^{3} \mathrm{Im}[n] \in ((\mathrm{Ri} - \mathrm{Gi} - \nabla\mathrm{RGB} < Rr - Gr < Ri - Gi + \nabla RGB) \wedge (\mathrm{Gi} - \mathrm{Bi} - \nabla\mathrm{RGB} < Gr - Br < Gi - Gi + \nabla RGB)) \quad 18$$

d) If the above condition is fulfilled, a new image is defined with the real colors detected in the image (Equation (19)):

$$Im_f[n] \leftarrow Rr$$
$$Im_f[n+1] \leftarrow Gr \quad (19)$$
$$Im_f[n+2] \leftarrow Br$$

If not, the information on the real color is not useful (Equation (20)):

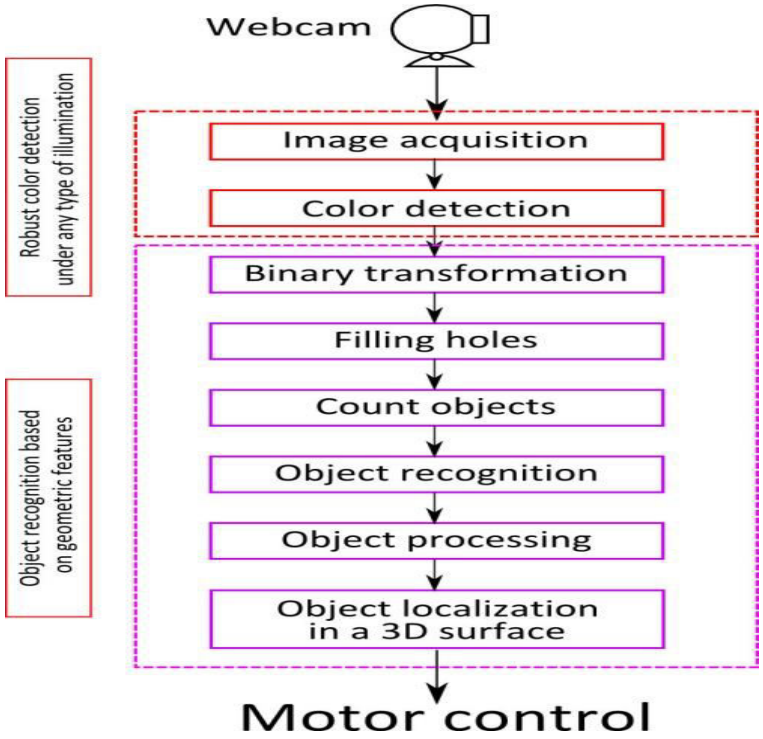

Figure-8. Structure of KUBO's vision algorithm for detecting balls.

$$\mathrm{Im_f}[n] \leftarrow 0$$
$$\mathrm{Im_f}[n+1] \leftarrow 0 \quad (20)$$
$$\mathrm{Im_f}[n+2] \leftarrow 0$$

Finally, the output of the algorithm is a color filter of same dimensions as the original image, in which only those colors within the range established by the gradient are retained. The rest of the image -which has no useful information- is set to black.

B) Object recognition

Once the color of an object has been detected, a particular shape can be recognized among several same-color-objects using morphological algorithms [18].

Consider the images acquired by KUBO's camera shown in Figures-9 and 10. Note that they exhibit different types of external illumination (Figures-9(a) and 10(a)).

Gradient ∇RGB allows detecting the target color (Figures-9(b) and 10(b)). The resulting image is then binarized to ease pattern recognition by means of morphological processes (Figures-9(c) and 10(c)).

Exterior illumination often produces white reflections and flashes on the objects which are not detected as part of the object by the color detection stage. After binarization, these reflections and flashes may remain as black pixels in the objects. A filling holes process solves this problem by completing the objects' shapes and by eliminating noisy pixels produced in the binary transformation (Figures-9(d) and 10(d)).

Image is then erode with a disk-like structural element to eliminate those objects whose shape is not a disk and to determine if the object is a ball or not. The result is dilated to reconstruct the ball (Figures-9(e) and 10(e)).

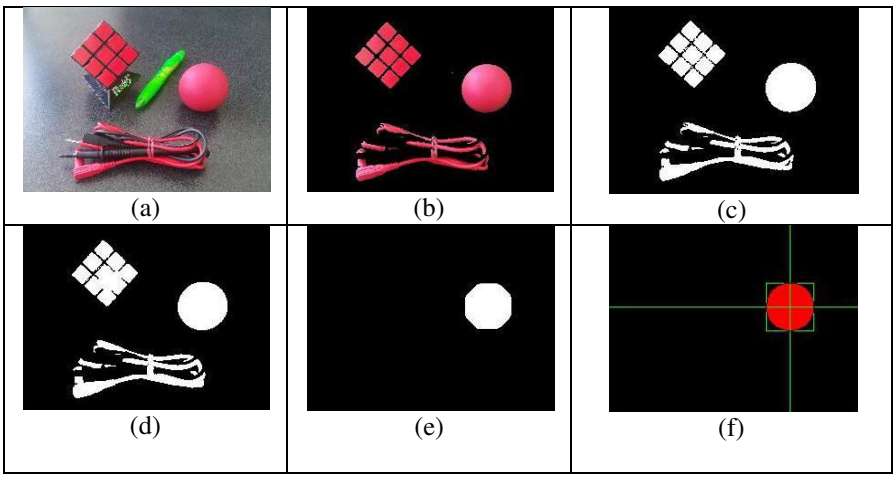

Figure-9. Identification of balls in normally lighted environments: (a) original image, (b) color detection, (c) binary image, (d) filling holes, (e) shape detection, and (f) ball located.

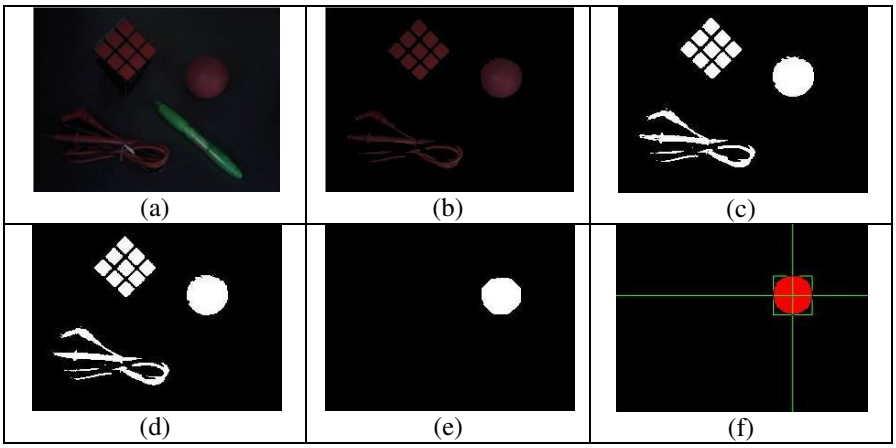

Figure-10. Identification of balls in dark environments: (a) original image, (b) color detection, (c) binary image, (d) filling holes, (e) shape detection, and (f) ball located.

Finally, this second stage of the algorithm proceeds to find the ball's centroid to determine its position in the environment (Figures 9(f) and 10(f)). With this information, KUBO is capable of determining the direction and the speed of the ball and sets these data as initial conditions for its motors with the aim of pursuing the ball.

5. CONCLUSIONS

This paper has introduced humanoid robot KUBO, a self-developed platform for bipedal walking research. KUBO is a 20-DOF robot capable of performing a wide number of movements. It includes a powerful on-board processing unit, on-board batteries, and a set of sensors that are currently being be exploited for standing balance, walking control, and autonomous motion.

A consistent methodology for deriving the forward kinematic analysis to determine the position of arms and legs was presented. Computer simulations have illustrated the robot's effective workspaces.

A computer vision algorithm for detecting balls was presented. This algorithm offers robust color and shape detection for efficient soccer playing. KUBO has participated in the two past editions of the Robocup: 2015 (Hefei, China) and 2016 (Leipzig, Germany). It is expected to participate in the 2017 edition of the same competition (Nagoya, Japan).

Computer vision algorithms inspired from previous work [19-21] are currently being developed for coarse manipulation, trajectory following, and human-computer interaction together with the integration of a novel nanocomposite optical sensor [22] for object scanning. Future work will focus on exploiting the derived models in this paper for establishing precise positioning control schemes.

REFERENCES

[1] Kagami S., Nishiwaki K., Kuffner J., Kuniyoshi Y., Inaba M. and Inoue H. 2002. Online 3D vision, motion planning and bipedal locomotion control

coupling system of humanoid robot: H7.Proc. of IEEE International Conference on Intelligent Robots and Systems. pp. 2557-2563.

[2] Loffler K., Gienger M. and Pfeiffer F. 2003. Sensor and control design of a dynamically stable bipe robot. Proc. of IEEE International Conference on Robotics and Automation. pp. 484-490.

[3] Kaneko K., Kanehiro F., Kajita S., Hirukawa H., Kawasaki T., Hirata M., Akachi K. and Isozumi T. 2004. Humanoid robot HRP-2. Proc. of IEEE International Conference on Robotics and Automation. pp. 1083-1090.

[4] Hirai K., Hirose M., Haikawa Y. and Takenaka T. 1998. The development of Honda humanoid robot. Proc. of IEEE International Conference on Robotics and Automation. pp. 1321-1326.

[5] Kuroki Y., Ishida T., Yamaguchi J., Fujita M. and Doi T. 2001. A small biped entertainment robot. Proc. of IEEE International Conference on Humanoid Robots. pp. 181-186.

[6] Kondo Kagaku Co. Updated information available at: http://kondo-robot.com/(last access July 2017).

[7] Aldebaran Robotics. Updated information available at: http://www.aldebaran-robotics.com/(last access July 2017).

[8] Innovati Inc. Updated information available at: http://en.innovati.com.tw/(last access July 2017).

[9] Ha I., Tamura Y., Asama H., Han J. and Hong D. 2011. Development of open humanoid platform DARwIn-OP. Proc. of SICE Annual Conference. pp. 2178-2181.

[10] Mittal R., Konno A. and Komizunai S. 2015. Implementation of HOAP-2 humanoid walking motion in OpenHRP simulation. Proc. of International Conference on Computing, Communication, Control and Automation. pp. 29-34.

[11] Hernandez E. and Velazquez R. 2011. Design and development of humanoid robot ZERO. Proc. of IEEEL at in American Robotics Symposium. pp. 1-6.

[12] Hernandez E. and Velazquez R. 2014. Diseño mecánico y análisis cinemático del robot humanoide AXIS. Pistas Educativas. 108, pp. 1102-1123.

[13] Robotis Co, Ltd., Updated information available at : http://www.robotis.us/dynamixel/ (last access July 2017).

[14] Rodríguez R., Chavarro A., Tovar M.A., Leiva A. and Ortiz L.F. 2017. Kinematic modelling of a robotic arm manipulator using Matlab. ARPN Journal of Engineering and Applied Sciences. 12(7): 2037-2045.

[15] Paul R., Shimano B. and Mayer E. 1981. Kinematic control equations for simple manipulators. IEEE Transactions on Systems, Man and Cybernetics. 11, pp. 449-455.

[16] Kitano H. and Asada M. 1998. RoboCup humanoid challenge: that's one small step for a robot, one giant leap for mankind. Proc. of IEEE International Conference on Intelligent Robots and Systems. pp. 419-424.

[17] Sulle B., Adriansyah A. and Dewi S. 2015. Coordination of mobile-robot system with behavior based architecture. ARPN Journal of Engineering and Applied Sciences. 10(16): 7179-7183.

[18] Banu A.S. and Vasuki P. 2015. Video based vehicle detection using morphological operation and hog feature extraction. ARPN Journal of Engineering and Applied Sciences. 10(4): 1866-1871.

[19] Farías V., Solis L., Meléndez L., García C. and Velazquez R. 2009. A four-fingered robot hand with shape memory alloys. Proc. of IEEE Africon. pp. 1-6.

[20] Romero B., Camacho A., Varona J., Delgado-Mata C. and Velazquez R. 2009. A low-cost electric power wheelchair with manual and vision-based control systems.Proc. of IEEE Africon. pp. 1-6.

[21] Pissaloux E., Maybank S. and Velazquez R. 2013. On image matching and feature tracking for embedded systems: a state of the art. In: A. Chatterjee, H. Nobahari & P. Siarry (Eds.), Advances in Heuristic Signal Processing and Applications, Springer (Berlin-Heidelberg). pp. 357-380.

[22] Giannoccaro N.I., Lay-Ekuakille A., Spedicato L., Massaro A. and Velazquez R. 2016. An innovative tool for detection of small notches using a nanocomposite optical sensor. IEEE Sensors Journal. 16(12): 5029-5036.